BB

GANIL

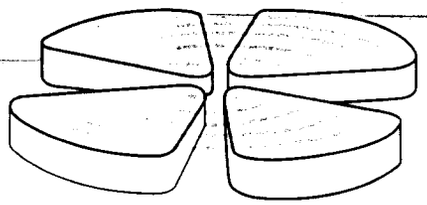

Decay Patterns of Target-like and Projectile-like Nuclei produced in $^{84}Kr + {}^{197}Au, {}^{nat}U$ Reactions at E/A = 150 MeV

B.M. Quednau [a,1], E. Crema [c], J. Galin [a], B. Gebauer [b], D. Hilscher [b], D. Jacquet [d], U. Jahnke [b], X. Ledoux [a], A. Lepine-Szily [a,c], S. Leray [f], B. Lott [a], M. Morjean [a], A. Péghaire [a], L. Pienkowski [f,2], S. Proschitzki [d], G. Röschert [b], H. Rossner [b], R.H. Siemssen [e], C. Stéphan [d]

[a] *GANIL(IN2P3-CNRS,DSM-CEA), BP 5027, F-14021 Caen Cedex*

[b] *Hahn-Meitner-Institut, Glienicker Str. 100, D-14109 Berlin*

[c] *IFUSP, DFN CP20516, 01498 São Paolo, S.P., Brazil*

[d] *IPN Orsay, BP 1, F-91406 Orsay Cedex*

[e] *KVI, NL-9747 AA Groningen*

[f] *LN Saturne(IN2P3-CNRS,DSM-CEA), F-91191 Gif-sur-Yvette Cedex*

GANIL P 96 10

Decay Patterns of Target-like and Projectile-like Nuclei produced in ^{84}Kr + ^{197}Au,^{nat}U Reactions at E/A = 150 MeV

B.M. Quednau [a,1], E. Crema [c], J. Galin [a], B. Gebauer [b], D. Hilscher [b], D. Jacquet [d], U. Jahnke [b], X. Ledoux [a], A. Lepine-Szily [a,c], S. Leray [f], B. Lott [a], M. Morjean [a], A. Péghaire [a], L. Pienkowski [f,2], S. Proschitzki [d], G. Röschert [b], H. Rossner [b], R.H. Siemssen [e], C. Stéphan [d]

[a] *GANIL(IN2P3-CNRS,DSM-CEA), BP 5027, F-14021 Caen Cedex*

[b] *Hahn-Meitner-Institut, Glienicker Str. 100, D-14109 Berlin*

[c] *IFUSP, DFN CP20516, 01498 São Paolo, S.P., Brazil*

[d] *IPN Orsay, BP 1, F-91406 Orsay Cedex*

[e] *KVI, NL-9747 AA Groningen*

[f] *LN Saturne(IN2P3-CNRS,DSM-CEA), F-91191 Gif-sur-Yvette Cedex*

Abstract

The reactions ^{84}Kr+^{197}Au and ^{84}Kr+^{nat}U were studied at an incident energy of E/A=150 MeV employing the large-volume neutron multiplicity meter ORION. The observed correlations between the atomic number of projectile-like nuclei (PLN) and neutron multiplicity indicate large deposits of excitation energies in the primary fragments. Angular correlations between fragments from the fission of target-like nuclei (TLN) and secondary PLN show a memory of the reaction plane. No indications for spin effects were found in the TLN-fission fragment distribution.

PACS: 25.75.+r, 25.70.Mn, 25.85.-w

Keywords: Relativistic heavy-ion collisions. E/A = 150 MeV. Kr + Au,U. Neutron Multiplicities. Energy dissipation. Fission probabilities.

[1] supported in part by a "Human Capital and Mobility" fellowship of the Commission of European Communities.

[2] permanent address: Heavy Ion Laboratory Warsaw University, 02-097 Warsaw, ul Banacha 4, Poland

1 Introduction

For many years now, production of hot nuclei and the study of their decay have been in the focus of interest of intermediate-energy heavy-ion experiments[1]. The fact that large amounts of kinetic energy can be dissipated in heavy-ion collisions and the prospect of being able to study thermal limits of stability of nuclei strongly motivated such studies. For this high excitation-energy regime new decay processes are predicted[2–5], e.g. multi-fragmentation, vaporization, and explosion-like reactions, which, if confirmed, are of great interest to the study of properties of nuclear matter. The use of heavy projectiles, however, does complicate the interpretation of experimental data because of large dynamical effects and the excitation of not only intrinsic degrees of freedom but collective ones as well, e.g. compression, deformation, rotation.

This work is part of a series of experiments using different types of projectiles(light ions [6], heavy ions[7], and $\bar{p}$[8]) which are used to examine separately, purely thermal decay and, by comparison, the effect of collective excitation. The experiment presented in this work using Kr-projectiles[9] and heavy targets was designed to study the decay of so called "spectator" nuclei[10] produced in peripheral collisions at high incident energies ($E/A > 100$ MeV). At these bombarding energies the "spectator" nuclei which in the following will be labelled as projectile-like(PLN) and target-like nuclei(TLN) are assumed to be produced with little compression, excitation, and spin because the reaction is dominated by nucleon-nucleon collisions while mean field effects vanish. This assumption leads to the simplified picture of non-communicating participant and spectator nucleons. However, experiments have shown that the participant-spectator reaction picture is much too simple and PLN and TLN can be very efficiently heated during the collision process [11–14]. In order to address the problem of underlying reaction and dissipation mechanisms in such collisions, the presented experimental work intended to determine the thermal excitation energy deposition via a measurement of the multiplicity of evaporated neutrons. The influence of angular momentum generated in fissioning TLN was to be estimated studying [15] the correlation between fission-fragment plane and reaction plane defined by the deflection direction of the coincident projectile-like nuclei.

2 Experimental Procedure

The experiment was performed at the SPES IV spectrometer beam line of the national laboratory SATURNE at Saclay, France, using a ^{84}Kr beam of E/A=150 MeV. A variety of thin $1.5\frac{\text{mg}}{\text{cm}^2}$ ^{197}Au, $0.6\frac{\text{mg}}{\text{cm}^2}$ $^{\text{nat}}$U and thick $192\frac{\text{mg}}{\text{cm}^2}$ ^{197}Au, $284\frac{\text{mg}}{\text{cm}^2}$ $^{\text{nat}}$U targets were used for exclusive and inclusive measurements

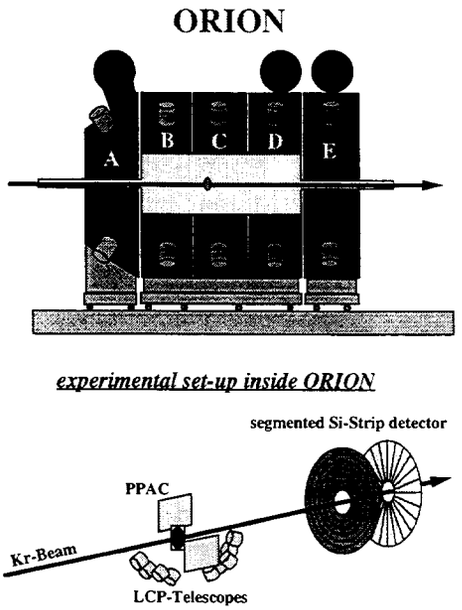

Fig. 1. Schematic drawing of the experimental setup. The upper part of the figure shows the segmented neutron multiplicity meter ORION. The lower part of the figure shows the setup inside the reaction chamber of ORION.

of neutron multiplicities, respectively. Neutron multiplicities were measured on an event-by-event basis with the large-volume neutron multiplicity meter ORION[16]. The detector consists of a vessel containing $4m^3$ of Gadolinium-doped liquid scintillator surrounding completely a scattering chamber containing the target and a number of charged product detectors (see Fig.1). The scintillator vessel is segmented into 5 independently operated detectors (in the following referred to as sections A to E) allowing a rough determination of the angular distribution of emitted neutrons. The effective electronic detection thresholds were typically set to values corresponding to gamma ray energies of 2-2.5 MeV. The resulting efficiency (ϵ) of the detector to neutrons emitted from a ^{252}Cf source was typically $\epsilon \approx 75\%$. The response of the detector to neutrons of higher energies was simulated using the Monte-Carlo code DENIS[17], which calculates the slowing-down, diffusion, and the Gd-capture of neutrons in the scintillator. According to these calculations, the capture probability for high-energy neutrons from the projectile is small, e.g. $\epsilon \approx 10\%$ for E_n=100 MeV.

Fragments from the fission of target-like nuclei were identified by energy loss and relative time-of-flight between fragments using a set of position sensitive parallel-plate avalanche counters (PPAC). The PPACS were placed parallel to the beam axis each at a distance of 60 mm. The angular range covered by the PPACs was 50 *deg* $\leq \Theta \leq$ 100 *deg* and 56 *deg* $\leq \Theta \leq$ 108 *deg* with an effective solid angle of 728 *msr* and 785 *msr*, respectively. The detection position was measured with a precision of $\Delta x \approx$ 1mm resulting in an angular resolution of $\Delta\Theta \approx \Delta\Phi \approx 1$ *deg*. Fig. 2 shows the correlation between relative time-of-flight

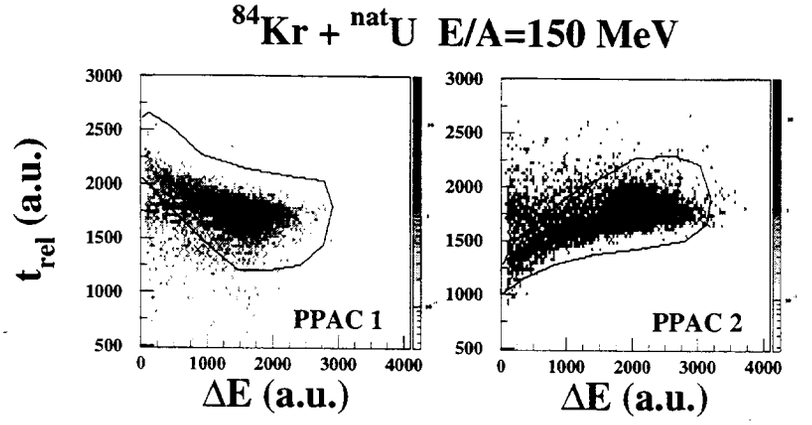

Fig. 2. Plot of energy loss ΔE vs. relative time-of flight t_{rel} between coincident fission fragments for PPAC1 and PPAC2. The solid contour lines encircle those events which were identified as fission fragments.

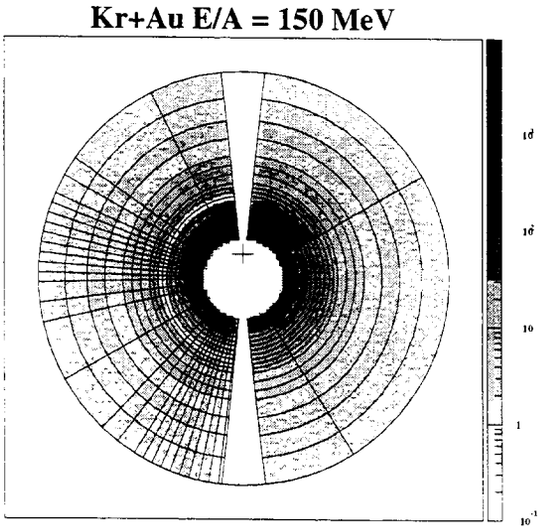

Fig. 3. Intensity hit-pattern of fragments detected with the forward angle Si-multi-strip detector. The reconstructed beam axis is perpendicular to the paper plane and indicated by a cross near the center of the figure. Circular segments indicate the partition of circular and radial detector segments. White areas represent inactive zones of the detector.

of two coincident fission fragments t_{rel} and the energy loss, ΔE, in the PPAC. The solid line represents the region used to define a fission fragment.

Projectile-like nuclei (PLN) were detected using a set of two Si-multi-strip detectors. The foremost detector had a thickness of 160μm and was divided vertically into two halves of 19 circular strips each with opening angles of 0.1 *deg* to 0.7 *deg*. The angular range covered by the detector was $\Theta = 0.5$ *deg*

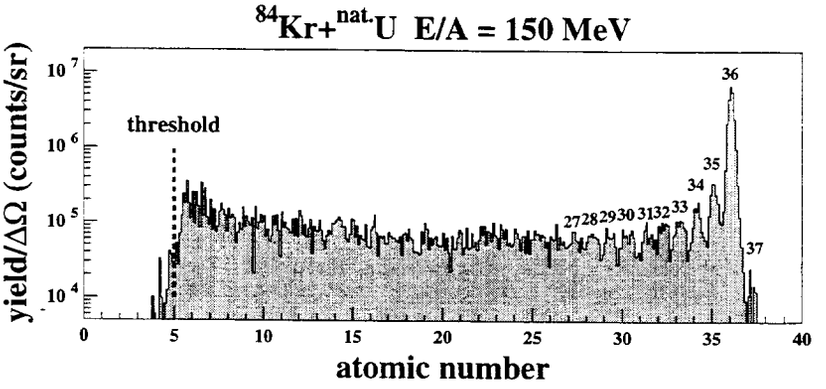

Fig. 4. Atomic-number distribution of fragments detected at $\Theta_{lab} = 1.4$ *deg*.

to $\Theta = 5.5$ *deg* including the grazing angle at $\Theta_{graz} \approx 0.9$ *deg*. The backward 520-μm-thick detector was subdivided into radial 32 segments with opening angles between $\Delta\Phi = 2.8$ *deg* to 87 *deg*. The particular partition geometry of the detector combination is displayed superimposed to the measured fragment distribution in Fig. 3. The gray-levels indicate hereby the number of counts detected in a given Θ and Φ-bin. As can be seen from the intensity distribution, the beam axis was found to be offset by about 4.5 mm from the symmetry axis of the Si-detector as was inferred from the measured intensities for elastic scattering by reconstructing isobaric levels of cross section. All PLN-angles quoted in the following are corrected for this offset.

The combination of two ΔE-Si detectors allowed for fragments traversing both detectors not only the measurement of scattering and azimuthal angles, but atomic numbers of PLNs as well. As can be seen from Fig. 4 Z-identification was possible between Z=37 and Z$\approx$27. Because PLN fragments move with approximately the same high velocity, separation of different Zs was possible by measuring the energy loss in one of the ΔE-Si detectors. For smaller impact parameter, i.e. on the average smaller Z, fluctuations in velocity of PLN become more important, leading to an increase in the width of the energy loss distribution for a given Z. Smaller Z-values quoted in the following could not be resolved but were extrapolated based on energy loss curves[18] and, therefore, are considered to be approximate mean values. The latter restriction, however, does not influence conclusions drawn from the data in the following.

Light-charged particles and intermediate-mass fragments were detected using a set of 9 Si-diode telescopes with typical thicknesses of $24\mu m/300\mu m$ $/5000\mu m$ or $12\mu m/80\mu m/500\mu m/5000\mu m$ placed at laboratory angles of $\Theta =$ 15 *deg* to $\Theta = 150$ *deg* in steps of $\Delta\Theta = 15$ *deg* covering a solid angle of 2.5 msr each. These detectors allowed the identification of Z=1 and Z=2 isotopes.

3 Theoretical Calculations

The experimental results presented in the following will be interpreted within the framework of theoretical model calculations. Seen from a technical point-of-view the simulation calculations serve to generate physically meaningful neutron velocity distributions. These predictions about the angular and energy distributions of neutrons are an important ingredient for the calculation of the average detection efficiency. Especially contributions to the measured neutron multiplicity originating from neutrons emitted during the fast cascade stage of the reaction and those evaporated from projectile-like and target-like nuclei depend much on efficiency simulations. Emission of pre-equilibrium particles (PEP) as well as excitation energies of fragments, however, are not well known and only few data exist in literature[19]. As it will become clearer in the following, the presented data are sensitive to neutrons emitted either way, such that a certain ambiguity concerning the consistency of the model predictions with the data cannot be resolved.

The theoretical calculations comprise four steps. The reaction was simulated by intranuclear cascade calculations, followed by a statistical decay of the excited PLN and TLN fragments. The cascade stage of the collision was described with the ISABEL code [20] after which the deexcitation of residual fragments was simulated with GEMINI[21] assuming a level density parameter of a=A/10 and spin I=0. The resulting set of simulated reaction events was then filtered with the geometrical acceptance of the charged particle detectors. The response of ORION to neutrons was calculated in two steps. Because those neutrons and charged particles, emitted with rather high kinetic energies during the INC cascade or being evaporated from the fast-moving projectile, may generate additional neutrons through secondary reactions in the scintillator itself and in the environment of the experimental set-up (concrete walls, floor and sealing, scattering chamber walls, lead shielding) the neutron yield will be enhanced. The generation of secondary particles as well as the back-scattering of neutrons into the detector was estimated employing GEANT/FLUKA[22]. Thereby, most of the additionally observed neutron yield is predicted to be generated by PEP inside the scintillator material or within the walls of the scattering chamber. The results were then corrected for the neutron detection efficiency with the code DENIS. Taking into account production of secondary neutrons in the simulation calculations proves to be important to the neutron yield measured in the most forward sections of ORION, i.e. D and E. The additional neutron yield calculated by these simulations amounts to $\approx$ 30% integrated over all sections and 15%, 50%, and 100% for sections C, D, and E, respectively.

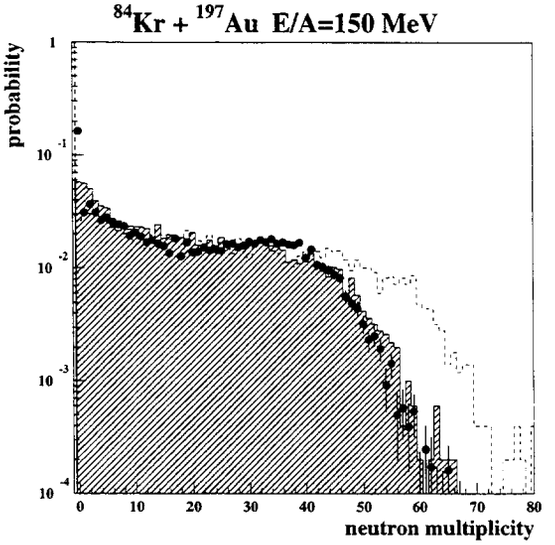

Fig. 5. Inclusive neutron multiplicity distribution for Kr + Au reactions. The neutron multiplicities are not corrected for efficiency but deconvoluted from the random background distribution. Results of simulation using excitation energies as predicted by ISABEL are represented by a dashed line. The hatched area corresponds to results of a calculation using reduced values of $E^* = 0.4 \cdot E^*_{ISABEL}$.

4 Experimental Results and Discussions

4.1 Measurement of Total Reaction Cross Sections

Inclusive neutron multiplicity measurements were performed using thick ^{197}Au and thick ^{nat}U targets and a low-intensity beam of about $1000s^{-1}$. The reduced beam intensities allowed the tagging and counting of beam particles using a thin plastic-scintillator detector of 1.4 mm thickness placed in the beam axis approximately 32m upstream of the target. From this detector a START-signal was generated in order to measure the time between the beam particle passing the detector and its arrival on the target followed by the induction of a nuclear reaction which is indicated by a prompt-response of ORION. This condition imposes a minimum bias on the type of selected reaction events, because ORION responds even to a single gamma ray (E_γ or $\sum_i E_{\gamma i} > 2.5$ MeV) emitted in very peripheral reactions. Based on this measurement total reaction cross sections of σ_{react}= 7.5 barns and σ_{react}=7.6 barns were obtained for the Kr+Au and Kr+U reactions, respectively. These values are close to the geometrical cross sections of 6.3 b and 6.7 b calculated from systematics [23] for Kr + Au and Kr + U reactions.

Fig. 5 shows the inclusive probability distribution for measuring a given neu-

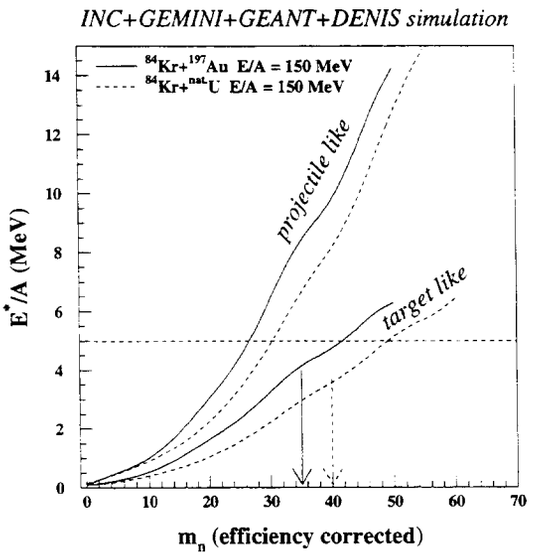

Fig. 6. Excitation energy in the target and projectile nuclei as a function of the total neutron multiplicity as predicted by the simulation calculations. The calculated neutron multiplicities are corrected for the detection efficiency. The vertical arrows indicate the average neutron multiplicities associated with the bump in Fig. 5 associated with central collisions.

tron multiplicity in the Kr + Au reaction (solid dots). The distribution was generated deconvoluting the measured multiplicity distribution with the multiplicity distribution for events not correlated with a reaction event thus, subtracting the random counting background. The probability distribution is peaked at low multiplicities decreasing exponentially with increasing neutron multiplicity, a characteristic that reflects the strong decrease of reaction cross section with impact parameter. A broad second maximum is observed for high neutron multiplicities associated with central collisions. These characteristics are very similar to those measured for heavy-ion reactions at lower bombarding energies [24,25].

The dashed line in Fig. 5 represents results of theoretical simulation calculations discussed above. The calculations over-estimate the cross section for large neutron multiplicities indicating that either the predicted average excitation energies in TLN and PLN or the multiplicities of PEP or both are too large. A quite good agreement can be obtained if the excitation energy is simply reduced by a factor ≈ 0.4, i.e. $E^* = 0.4 \cdot E^*_{\mathrm{ISABEL}}$. *Only results of simulations using these reduced excitation energy values will be presented in the following!* Latter excitation energies should only be considered to give a rough indication of the over-estimation by the ISABEL code rather than to give exact predictions of excitation energies because PEP multiplicities were not changed in the simulation. The results of the calculation are represented by the hatched area in Fig. 5.

The resulting relation between calculated, efficiency corrected neutron multiplicity and excitation energy in projectile-like and target-like nuclei is displayed in Fig. 6 for the Kr+Au and Kr+U reactions. For both reactions a flat slope is found at low neutron multiplicities due to the low binding energy for neutrons in neutron-rich target-like nuclei. For high neutron multiplicities a steeper slope and an almost linear correlation between E^*/A and m_n is observed. The excitation energy per nucleon is proportional to the number of abraded nucleons ΔA. For PLN an increase of $E^*/A\ |_{PLN} = 0.22\text{MeV} \cdot \Delta A_{PLN}$ is calculated while the excitation energy in the the much heavier TLN increases $E^*/A\ |_{TLN} = 0.12\text{MeV} \cdot \Delta A_{TLN}$.

4.2 Multiplicities of Alpha-Particles

Cross sections for the production of light charged particles were determined for alpha-particles emitted to backward angles, i.e. 150 *deg*, 135 *deg*, and 120 *deg*. For all other scattering angles and for the hydrogen isotopes not all particles were stopped in the detector so that a significant part of the yield could not be used for analysis. Since alpha-particle yields measured at very backward angles are relatively unaffected by contaminants from other contributions, e.g. PEP , the assumption of one single source for all the detected particles is well justified. Therefore, the integrated yield per solid angle in the the TLN emitter frame was computed for each detector telescope and extrapolated assuming isotropic emission to 4π in order to calculate the corresponding multiplicity of alpha-particles. The assumption about the velocity of the TLN needed for the transformation of the laboratory cross sections th the TLN emitter frame is based on the cascade calculations for Kr+Au which predict moderate recoil velocities of the TLN ($v_{TLN} = 0.3, 0.6, 0.7, 0.9$ cm/ns for bins m_n=20-35, 34-39, 40-45, 46-57, respectively). The reliability of the calculated velocities were confirmed by studies of fission fragment angular correlations measured for the Kr + U reactions which will be discussed further below.

Fig. 7 shows the alpha-particle multiplicities extrapolated from the measured yields at three angles for four different bins of neutron multiplicity. The size of the error bars shown in Fig. 7 is mostly due to statistical errors and estimated uncertainties of the normalization procedure, between inclusive measurements on thick targets and exclusive measurements on thin targets. Results of the simulation calculations are represented in Fig. 7 by the open squares. The calculated multiplicities have the tendency to overestimate the experimentally found ones but are consistent within the experimental error bars. Since alpha-particle emission is a very sensitive probe for high excitation energies (because they are unperturbed by PEP and their multiplicity depends strongly on E^*) this agreement gives another strong indication that the reduction of the TLN excitation energies introduced in the above calculations is indeed justified.

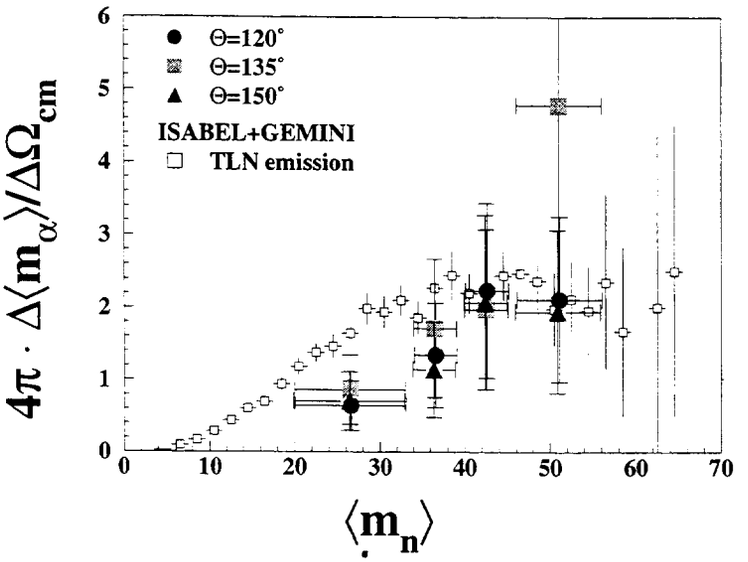

Fig. 7. Alpha-particle multiplicities extrapolated from the yield measured at discrete backward scattering angles as a function of neutron multiplicity. The open squares represent results of the simulation calculations.

4.3 Projectile-like Nuclei

Fig. 8 shows double differential cross sections of fragments, produced in Kr+Au collisions at E/A = 150 MeV, detected in the forward-angle multi-strip ΔE-ΔE Si-detector for 5 scattering angle bins. The distribution of fragments detected between $\Theta = 0.5\ deg - 1.5\ deg$, including the grazing angle for this reaction ($\Theta_{graz} \approx 0.9\ deg$), is displayed in the upper-left panel. Most prominent feature of this distribution is a group of elastically and quasi-elastically scattered projectiles, centered at atomic number Z=36 and neutron multiplicity $m_n = 0$, from which a continuous band of cross sections evolves with increasing average neutron multiplicity for decreasing Z. No qualitative change of the average correlation between atomic number of the projectile-like fragment and average neutron multiplicity as a function of scattering angle is observed. However, a strong change in the production cross-sections is seen. Fragments with large Z are strongly suppressed for larger scattering angles whereas low-Z fragments are distributed more evenly in the angular range between $\Theta = 0.5\ deg$ and $5.5\ deg$. The correlation between Z of the projectile-like nuclei and neutron multiplicity reflects the strong dependence of the size of the projectile-like nuclei and dissipated energy on the size of the overlap between target and projectile and thus, on impact parameter. Thus, neutron multiplicity appears to be a good observable to select an impact parameter or a degree of dissipation, at least for relatively peripheral collisions, as it was shown at much lower bombarding energies[16]. Because of electronic detection thresholds, fragments with atomic numbers of less than 5 were not measured. For the lightest frag-

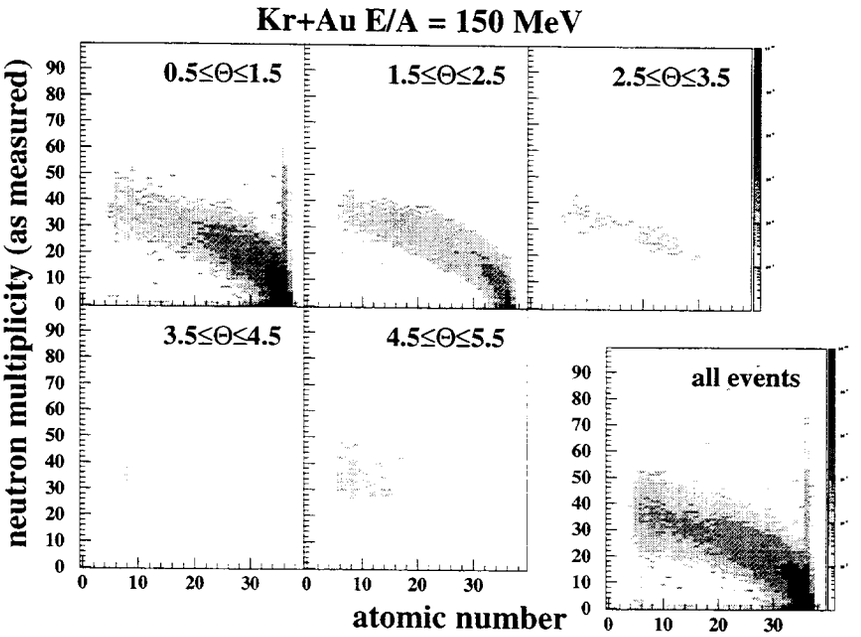

Fig. 8. Distributions of double-differential cross-sections for fragments produced in Kr+Au collisions at E/A = 150 MeV for six bins of scattering-angle. The logarithmic intensity scale is the same for all distributions and defined by gray levels. The intense line structure at Z=36 is a result of pile-up of reaction events with elastic scattering.

ments that were detected average multiplicities of $\langle m_n \rangle \approx 35$ are observed coinciding with the maximum observed in Fig. 5 for the most dissipative collisions. In this context, it is interesting to note that this pattern is quite similar to that already observed for the same system at a much lower bombarding energy of E/A=32 MeV[26].

Simulated neutron multiplicities are presented separately for each section of ORION in Fig. 9. As can be seen in this figure, the functional dependence of the average neutron multiplicity $\langle m_n \rangle$ on Z integrated over $\Theta = 0.5 - 5.5$ *deg* is quite well reproduced. A slight underestimate can be seen for the backward section B and the most forward section E. This disagreement, however, can not be taken as an unambiguous proof for the failure of the reaction model. It has to be kept in mind, that important corrections due to secondary neutron production were applied whose precision is difficult to estimate. Furthermore, although excitation energies predicted to be deposited in the TLN are mostly below $E^*/A = 5$MeV, the excitation energies in PLN may be much higher such that the mass loss predicted by GEMINI may be questioned. However, it can be concluded qualitatively that the amount of thermal excitation energy generated in the TLN and PLN produced in Kr+Au collisions at E/A=150 MeV is large (see also [12,13]). According to cascade calculations excitation energies

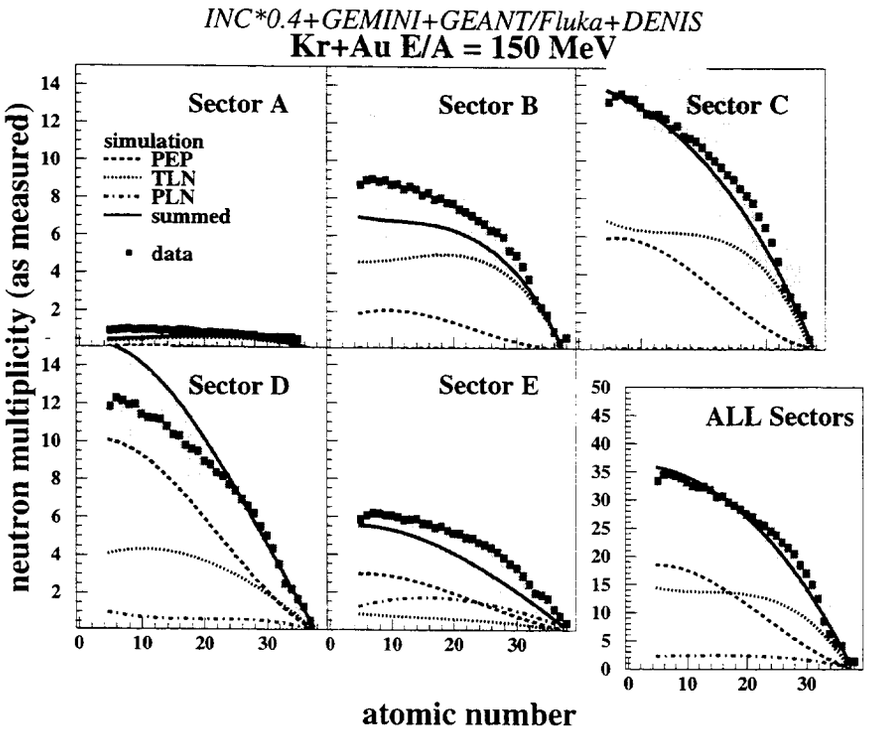

Fig. 9. Comparison between the simulation calculations and the experimental data for each section as a function of the atomic number of PLN's. The experimentally observed average neutron multiplicities as a function of the Z are represented by the filled squares. The filled area indicates the $\pm\sigma$-width of the experimental distribution. The averages predicted by the simulations are represented by a solid line. Contributions from TLN, PLN, and for PEP (Pre-Equilibrium Particles) are represented by broken lines(see upper left panel). The ingredients of the simulation calculation are described in the text.

in TLN of up to $E^*/A \approx 5$ MeV are reached for more central collisions while the associated excitation energies in the PLN may exceed $E^*/A \approx 10$MeV (see Fig. 6).

4.4 Fission of Target-like Nuclei

Fission of the target-like nuclei was studied for the Kr+U reactions as a function of the neutron multiplicity via a measurement of the fission probabilities and the angular correlations between fission fragments. Two correlation angles were examined. The distribution of folding angle ($\Theta_{fold} = \Theta_{ff1} + \Theta_{ff2}$) which is mostly sensitive to the parallel velocity of TLN and the distribution of the azimuthal folding angle $\Delta\Phi_{ff} = \Phi_{ff1} - \Phi_{ff2}$(see Fig. 10) in which the transverse velocity distribution is reflected. Fission probabilities were obtained from a comparison of the inclusively measured neutron multiplicity distribution with those obtained in coincidence with fission fragments. Because of finite coinci-

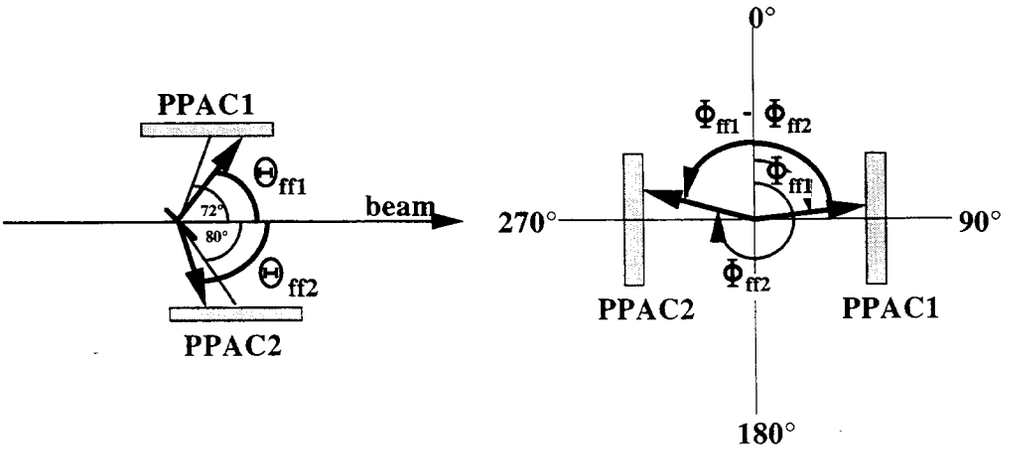

Fig. 10. Definition of angles used in the text.

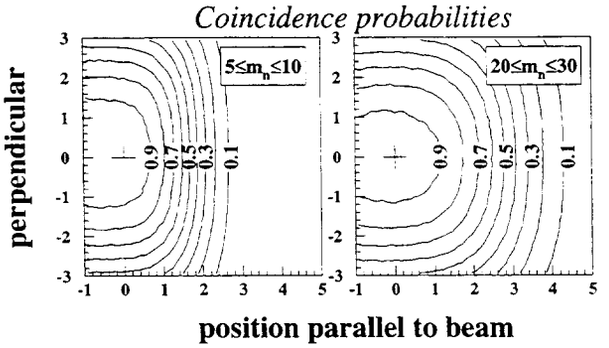

Fig. 11. Contour diagram of the coincidence probability as a function of impact position on PPAC2 parallel and perpendicular to the beam. The projected target position in indicated by a cross in the left corner at (0,0).

dence probabilities, however, efficiency corrections have to be applied to the calculations in order to obtain distributions that can be compared directly to experimental data.

4.4.1 Determination of Fission Probabilities

— Corrections for Finite Coincidence Probabilities

The influence of the geometry of the experimental setup on the detection probability for coincidences between fission fragments was estimated by means of Monte-Carlo simulations. Main ingredient of these simulations are measured widths of fission fragment distributions as a function of neutron multiplicity. These widths were determined by selecting a small area in the center of PPAC1 and computing the first two moments of the experimentally observed distribution of coincident fission fragments on PPAC2. These values were then used to calculate the detection efficiency for the full range of Θ and Φ cov-

m_n	ϵ_{geo}^{exp}	ϵ_{geo}^{sim}	$v_{TLN}/\frac{cm}{ns}$	$\Delta\Omega_{cm}/2\pi$	$\epsilon_{geo}^{exp} \cdot \Delta\Omega_{cm}/2\pi$
< 5	0.37	0.35	-0.2 ± 0.2	0.105	0.038
5-10	0.42	0.39	-0.2	0.105	0.042
10-15	0.44	0.42	0.0	0.116	0.044
15-20	0.53	0.54	0.0	0.116	0.062
20-30	0.51	0.50	0.1	0.120	0.062
> 30	0.30	0.54	0.3 ± 0.1	0.124	0.037

Table 1
Applied efficiency corrections for geometrical effects and solid angle correction for finite recoil velocity of fissioning TLNs.

ered by PPAC1. Results of the calculation are represented in form of a contour diagram in Fig.11. The left-hand side of Fig. 11 shows the probability distribution for detecting fission fragments in coincidence for low neutron multiplicity events associated with $5 < m_n < 10$. The distribution is peaked near the border of the PPAC. Moving forward parallel to the beam, i.e. for increasing Θ, the coincidence probability is rapidly decreasing. This effect is due to a folding angle near 180 *deg* which makes a coincidence geometrically impossible for a fragment detected in coincidence in the forward region of the PPAC. With increasing neutron multiplicity the average of the folding angle distribution decreases and its width increase which leads to a widening and a shift of the coincidence probability distribution towards small scattering angles as can be inferred from the plot on the right-hand side of Fig. 11. The calculations were verified by folding the impact position distribution of fission fragments for one PPAC measured in singles mode with the calculated efficiency matrix, and comparing it with impact position distribution measured for coincident fragments. A good agreement was found for all neutron multiplicities except for the largest energy dissipation (see Table 1). For this bin the efficiency was estimated to be too large which is most likely due to an underestimate of the measured width of the fragment distribution.

The recoil velocity of the fissioning target nucleus was inferred by fitting the inclusively measured angular distribution of fission fragments, assuming an isotropic emission in the rest frame of the target-like nucleus. These fits were performed for several neutron multiplicity bins. The values found for v_{TLN} are very small and may be zero within the estimated error for this kind of measurement, but they are comparable with predictions of INC calculations. Thus, the applied solid angle corrections are small compared to those due to the detection efficiency. The velocities resulting from these fits were then used to transform the solid angle of the PPAC to that of the TLN frame. The results

are plotted again in Tab. 1 for each neutron multiplicity bin. Negative values of velocity are compatible with $v_{TLN} = 0$ taking into account the precision of this method.

— *Normalization of Exclusive Measurements*

For the measurements performed with thin targets the flux of incident particles could not be determined directly, because of the much higher beam current ($10^6 - 10^7 s^{-1}$). Therefore a relative normalization between the two types of measurements had to be performed using quasi-elastically scattered projectiles (selected by requiring $m_n = 0$ and $Z = 36$) measured with the forward angle Si-strip detector telescope. Because of the very different target thicknesses used for inclusive and exclusive measurements, the angular distribution of quasi-elastically scattered fragments for thick-target runs is broadened significantly.

In order to take into account this effect, the angular distribution $\frac{d\sigma}{d\Omega}(\Theta)$ for thin target runs was expressed in the form of a function $f(\Theta)$ and folded with a gaussian resolution function[27] thus, correcting for small-angle scattering effects in the target and in the plastic beam-flux monitor detector. This functional dependence was then used to fit the normalization factor between inclusive and exclusive measurements. The uncertainty in the normalization factor was estimated to be 30-40% by varying $f(\Theta)$. With this relative normalization and applying efficiency corrections for each neutron multiplicity bin the fission probability can be calculated by dividing the number of fission events by the number of nuclear reactions for each neutron multiplicity bin.

The second column of Tab. 2 shows the experimental fission probability as function of neutron multiplicity. The excitation energy scale plotted on the right hand column was deduced from the simulation calculation discussed above (see Fig. 6). A strong increase of the fission probability with increasing neutron multiplicity is observed which reaches unity at $\langle m_n \rangle \approx 10$. Above $\langle m_n \rangle \approx 30$ the fission probability decreases again. According to the simulation calculations this decrease sets in at an excitation energy of about $E^*/A = 3MeV$ ($T \approx 5MeV$) but a measurable cross-section can be observed up to the highest excitation energies. The competition between fission and charged-particle emission or multi-fragment decays will increase in this excitation energy regime which may make fission more and more unlikely. The integrated fission probability was determined to be 47% or $\sigma_{fission} = 3.6$ b.

The third column of Tab. 2 shows the average atomic number of PLN associated with fission of the TLN measured as function of neutron multiplicity. The comparison with calculations shows a good agreement with the data indicating that the simulated reaction scenario on the average reproduces both, excitation energy and average size of PLN and TLN.

Experiment				Simulation			
m_n	P_{fiss}	$\langle Z_{PLN} \rangle$	σ_{PLN}	P_{fiss}^{calc}	$\langle Z_{PLN}^{calc} \rangle$	$E^*/A\|_{TLN}^{calc}$	$E^*/A\|_{PLN}^{calc}$
0.0	0.01 ± 0.001	36.0	0.4	0.65	36.0	0.1	0.2
2.0	0.27 ± 0.07	36.0	0.4	0.76	35.9	0.1	0.3
4.0	0.47 ± 0.13	35.9	0.4	0.87	35.2	0.2	0.5
6.0	0.60 ± 0.16	35.2	3.5	0.95	34.9	0.3	0.6
8.0	0.53 ± 0.16	35.0	2.5	0.96	34.5	0.4	0.8
10.	0.83 ± 0.21	34.6	3.3	0.94	34.5	0.5	1.0
12.	0.97 ± 0.26	34.4	1.6	0.93	34.0	0.6	1.2
14.	0.76 ± 0.23	33.4	2.0	0.86	33.7	0.6	1.5
16.	0.99 ± 0.26	32.4	2.0	0.79	32.7	0.8	1.9
18.	0.85 ± 0.25	32.0	2.5	0.83	31.2	1.0	2.1
20.	0.93 ± 0.27	30.9	3.9	0.77	29.7	1.1	2.5
22.	1.04 ± 0.29	29.7	4.6	0.77	28.6	1.3	2.8
24.	0.81 ± 0.25	29.4	5.3	0.55	27.3	1.5	3.4
26.	1.02 ± 0.28	26.9	5.8	0.42	26.0	1.9	3.9
28.	0.81 ± 0.25	25.8	5.9	0.33	24.8	2.0	4.5
30.	1.09 ± 0.34	23.2	6.2	0.21	23.7	2.3	5.0
32.	0.69 ± 0.31	22.6	6.1	0.28	21.2	2.7	6.0
34.	0.86 ± 0.29	21.1	7.0	0.29	18.9	2.7	6.5
36.	0.79 ± 0.26	20.6	6.5	0.28	19.3	3.1	7.0
38.	0.34 ± 0.19	18.3	6.9	0.19	15.9	3.5	8.4
40.	0.35 ± 0.20	18.1	5.2	0.21	15.9	3.8	8.9
42.	0.33 ± 0.16	18.4	5.6	0.06	15.7	4.1	9.7
44.	0.19 ± 0.19	15.0	5.7	0.10	16.7	4.5	10.6
46.	0.17 ± 0.12	17.7	6.9	0.04	15.8	4.7	11.5
48.	0.30 ± 0.15	14.0	4.7	0.06	12.7	4.8	12.0

Table 2
Fission probabilities and average secondary Z of the coincident PLN for Kr+U reactions as function of the detected number of neutrons. The experimental errors given for P_{fiss} do not include the systematic errors due to the normalization procedure. The two right columns contain predicted values of excitation energies in TLN and PLN.

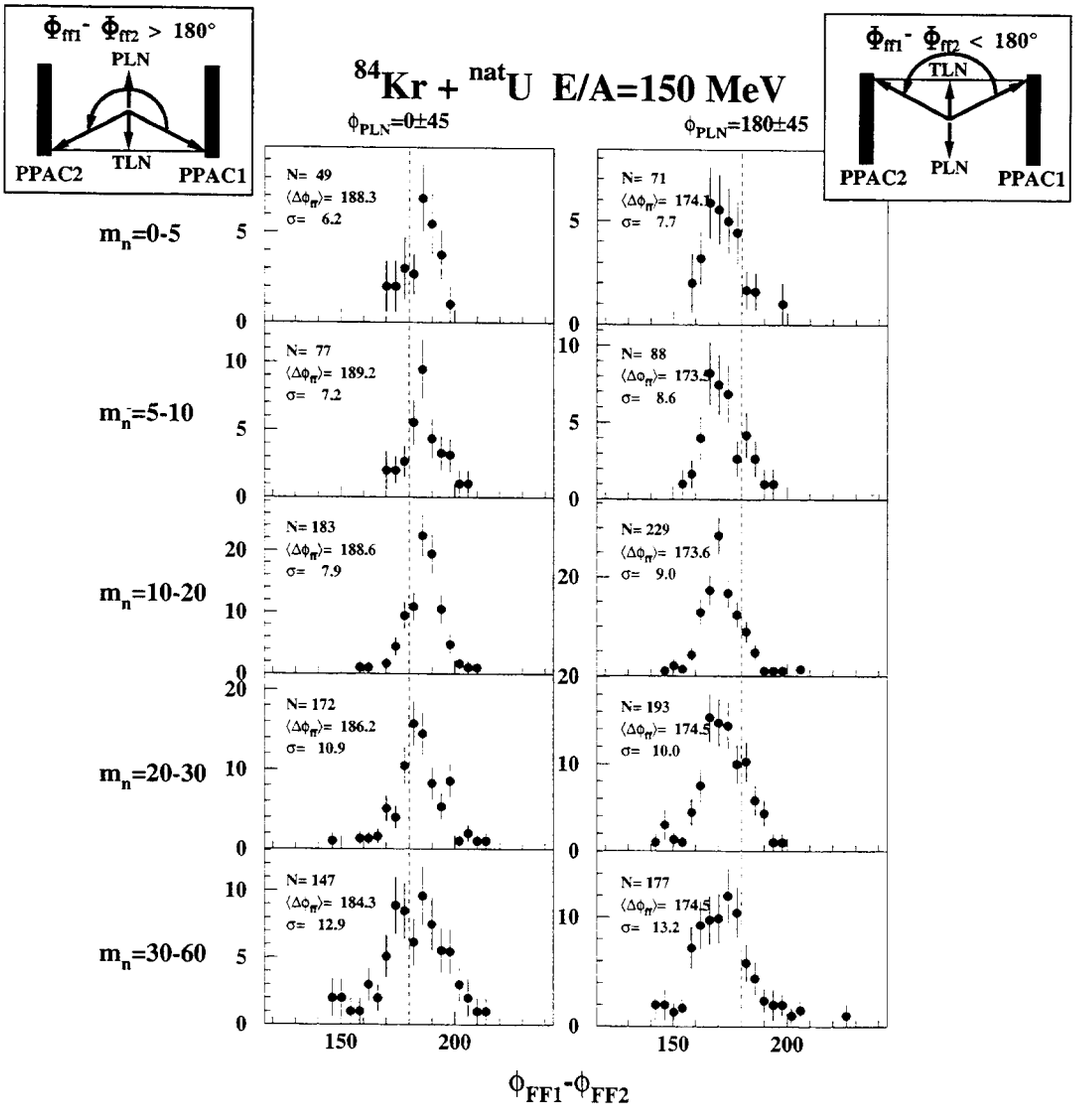

Fig. 12. Azimuthal folding-angle distribution of fission fragments as a function of neutron multiplicity in coincidence with projectile-like fragment nuclei. The range of the azimuthal angle for PLN for the left and right-hand column is indicated on the top of the figure, respectively.

4.4.2 Angular Correlations between Fission Fragments

The left-hand side of Fig.13 shows the folding angle ($\Theta = \Theta_{ff1} + \Theta_{ff2}$) distribution for pairs of fission fragments from the reaction ^{84}Kr + ^{nat}U as a function of neutron multiplicity. A continuous decrease of the mean folding angle with neutron multiplicity can be observed corresponding to increasingly larger recoil velocities of the fissioning TLN ($v_{TLN} \leq 0.4\frac{cm}{ns}$). The right-hand side of Fig. 13 shows the corresponding distributions of the azimuthal folding angle, i.e. $\Delta\Phi_{ff} = \Phi_{ff1} - \Phi_{ff2}$. The distribution is symmetrical with respect to $\Delta\Phi_{ff} = 180$ *deg* since no preferred fission-plane is selected. Though the first two moments of the distribution evolve only weakly with neutron multiplicity, a qualitative change of the distribution can be observed. At low neutron multiplicities the distribution appears relatively wide while the distribution

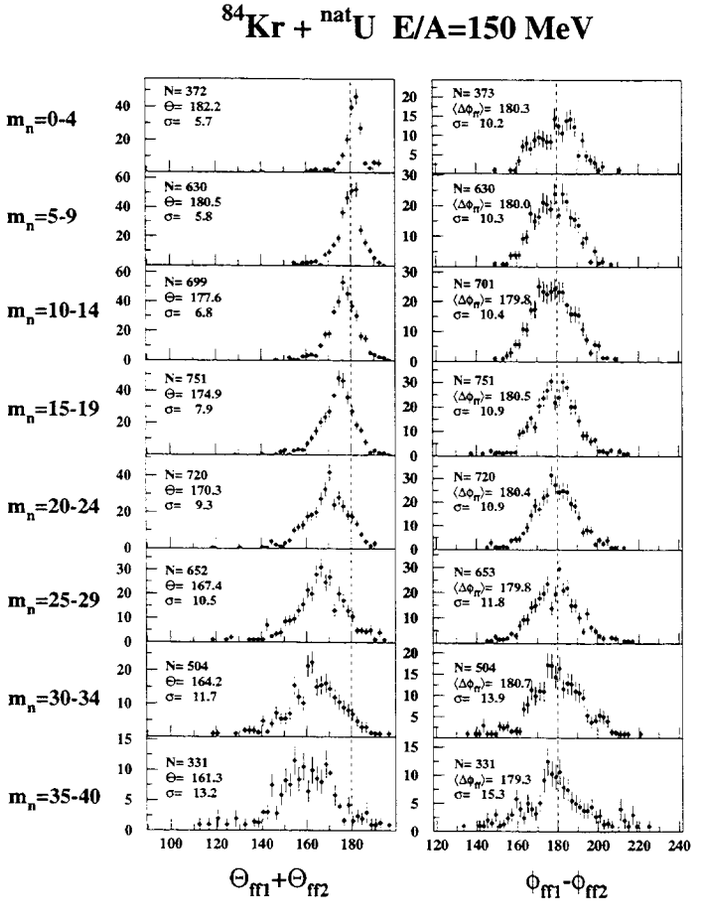

Fig. 13. Distributions of folding angle and azimuthal folding angle for fragments from the fission of target-like nuclei. The left-hand side shows the evolution of the folding angle with neutron multiplicity. The right-hand side displays the associated distributions of azimuthal angles. Number of events, mean angle, and standard deviation of the distributions are plotted in the respective panel.

becomes broader but has a pronounced maximum at $\Delta\Phi_{\rm ff} = 180$ *deg* for larger multiplicities. The relatively broad distribution for neutron multiplicities $m_n < 10$ indicates a significant average transverse velocity of the fissioning target-like residual nucleus. In order to search for the origin of this transverse velocity, triple coincidences between a projectile-like residue detected in the forward-angle Si-Strip detector and a pair of fission fragments were used to generate azimuthal angle correlations of the fission fragments. Fig. 12 shows these angular distributions as function of neutron multiplicity. Two types of coincidences were selected, where the transverse velocity vector of the PLN is on the average perpendicular to the fission plane, but pointing to opposite directions. The left-hand side shows the distribution for $\Phi_{\rm PLN} = 0$ *deg* ± 45 *deg* where the PLN vector points "upwards" (for orientation see inlets) the right-hand-side is associated with events where this vector points "downwards", i.e. $\Phi_{\rm PLN} = 180$ *deg* $\pm$ 45 *deg*. Although statistical errors are significant, a clear systematic shift of the average angle $\langle\Delta\Phi_{\rm ff}\rangle$ with respect to $\Delta\Phi_{\rm ff} = 180$ *deg*

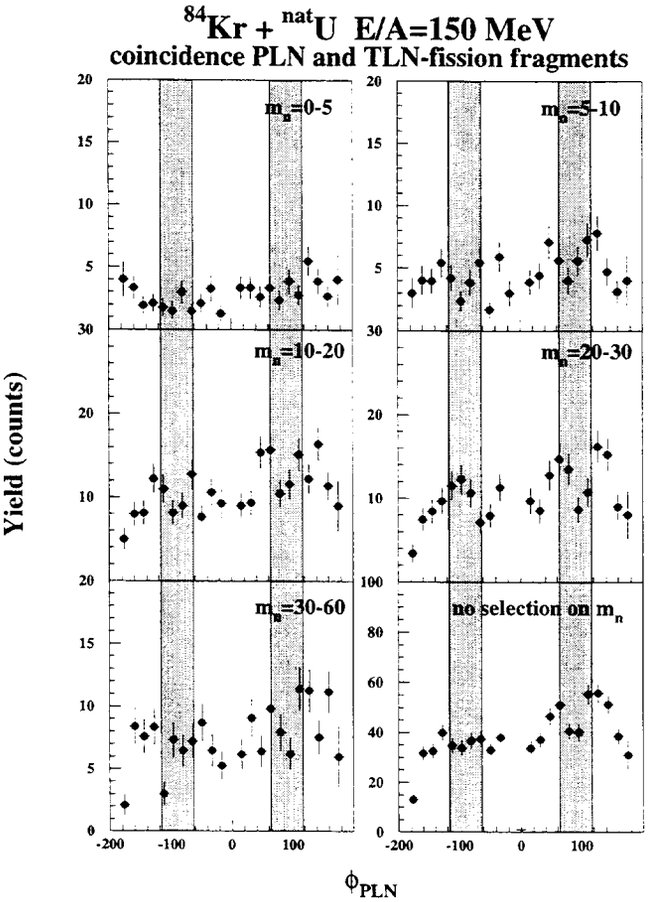

Fig. 14. Azimuthal angle distribution of PLN as function of multiplicity in coincidence with a pair of fission fragments. The azimuthal angular range covered by the PPACs is indicated by gray areas, which also defines the orientation of the fission plane.

can be seen whose sign depends on the direction vector of the PLN. This result shows that by selecting the PLN-direction one is able to select an average reaction plane, even for the largest neutron multiplicities. A priori, it was not evident that such a correlation could be found, since experimental errors, e.g. due to beam divergence, might have been sufficiently large to mask recoil effects. The ability to select the reaction plane is used in the following to search for spin effects in fission decay of the TLN by searching for correlations between fission and reaction plane.

4.4.3 Searching for Spin Effects in the Fission Decay of TLNs

Fig.14 shows as function of neutron multiplicity the azimuthal angular distribution of PLN in coincidence with a pair of fission fragments detected in the PPACs. Thereby, the PLNs direction is used to define the orientation of the reaction plane. If there was a strong alignment of reaction plane and fission

plane, the azimuthal angular distribution of the coincident PLNs would not be uniform but would have maxima around the Φ corresponding to the position of the PPAC indicated in Fig. 14 by the gray-shaded areas. However, within the statistical errors the distribution is not clearly structured, i.e. fission plane and reaction plane are not or only weakly correlated with each other as already observed at higher bombarding energies[28]. There are a number of possible explanations for such an observation. Firstly, the selection of the reaction plane may not be sufficiently precise, such that angular correlations are washed out. Secondly, spin generated in the nuclei may be small leading to essentially flat angular distributions of the fission fragments. Lastly, spin might be generated in a way that the reaction plane does not select the direction of the spin. In fact, the observation of an alignment of the nuclear spin and the normal vector of the reaction plane is a feature of the reaction mechanism whose tangential dissipation component leads to the generation of spin. Therefore, the non-observation of such an alignment may be taken as an indication that the mechanism of generating spin and excitation energy in residual nuclei may be quite different from, e.g. binary dissipative reactions prevailing at lower bombarding energy.

5 Summary

For the first time, neutron multiplicity distributions were measured for heavy-ion induced reactions at relativistic bombarding energies using a 4π neutron multiplicity meter. Average secondary Zs of PLN and alpha-particle multiplicities for Kr + Au are described qualitatively as a function of neutron multiplicity by calculations assuming an intranuclear cascade and evaporation from thermalized nuclei, provided that the predicted excitation energies are reduced by a factor 0.4. Average neutron multiplicities measured in coincidence with projectile-like nuclei exhibit a smooth evolution with atomic number and scattering angle. The experimental distributions show that large amounts of thermal energies (E^*/A up to 5 MeV) are deposited in the TLN. Fission of TLNs is observed in Kr + U up to high neutron multiplicities which are associated with excitation energies of more than $E^*/A = 3$MeV. The observed angular correlations between projectile-like and target-like nuclei allow a selection of the reaction plane. Within the experimental errors no indication of spin effects on the angular distribution of fission fragments were found.

Acknowledgement

The authors would like to thank G. Milleret for his valuable help in the optimization of the beam transport at the SPES IV beam line.

References

[1] D. Guerreau, in:*Nuclear Matter and Heavy-Ion Collisions*, eds. M. Soyeur, H. Flocard, B. Tamain and M. Porneuf (Plenum, New York and London, 1989), and references therein.

[2] J.P. Bondorf et al. Nucl. Phys. A443 (1985) 321, A444 (1985) 460.

[3] W. Bauer, G.F. Bertsch and S. Das Gupta, Phys. Rev. Lett. 58 (1987) 863.

[4] G. Fai und J. Randrup, Nucl. Phys. A381 (1982) 557, A404 (1983) 551.

[5] D.H.E. Gross et al. Phys. Rev. Lett. 56 (1986) 1544, Nucl. Phys. A461 (1987) 641, A461 (1987) 668.

[6] L. Pienkowski et al., Phys. Lett. B336, 147(1994)
X. Ledoux et al., Proc. 33rd Int. Winter Meeting on Nucl. Physics, Ed. I. Iori, Bormio, Italy, Jan 23-27, 1995, p. 406.

[7] B.M. Quednau et al., Proc. Int. Workshop XXII on Gross properties of Nuclei and Nuclear Excitations, Hirschegg, Austria, Jan. 17-22, 1994, p. 183.
B.M. Quednau et al., Proc. 33rd Int. Winter Meeting on Nucl. Physics, ed. I. Iori, Bormio, Italy, Jan 23-27, 1995, p. 306.

[8] D. Hilscher et al., Proc. LEAP Workshop, Bled, Slovenia,
ed. G. Kernel, P. Krizan, M. Mikuz (World Scientific 1995) p. 331.

[9] G.F. Peaslee et al., Phys. Rev. C49 (1994) R2271.

[10] G. Westfall et al., Phys. Rev. Lett. 37 (1976) 1202.

[11] C. Donzaud et al., Nucl. Phys. A593 (1995) 503.

[12] C. Stéphan et al., Phys. Lett. B262 (1991) 6.

[13] J. Pochodzalla et al., Phys. Rev. Lett. 75 (1995) 1040.

[14] M. Begemann-Blaich and Th. Blaich et al., Phys. Rev. C45 (1992) 677 and 689.

[15] D. v. Harrach et al., Phys. Rev. 42 (1979) 1728.

[16] J. Galin and U. Jahnke, J. Phys. G: Nucl. Part. Phys. 20 (1994) 1105.

[17] J. Poitou and C. Signarbieux, Nucl. Instr. Meth. 114 (1974) 113.

[18] J.F. Ziegler et al., *The stopping and Range of Ions in Solids*, Pergamon Press, New York, 1985.
F. Hubert et al., Atomic Data and Nucl. Data Tab., 46 (1990) 1.

[19] J. Gosset, H.H. Gutbrod, W.G. Meyer, A.M. Poskanzer, A. Sandoval, R. Stock and G. Westfall, Phys. Rev. C16 (1977) 629.

[20] Y. Yariv and Z. Fraenkel, Phys. Rev. C20 (1979) 2227, C24 (1981)488, K. Chen et al., Phys. Rev. 166 (1968) 949.

[21] R.J. Charity et al., Nucl. Phys. A483 (1988) 371.

[22] CERN Application Software Group, GEANT - Detector Description and Simulation Tool, CERN long writeup W5013, Geneva 1993.

[23] W. Wilcke et al., Atomic Data and Nucl. Data Tab. 25 (1980) 389.

[24] M. Morjean et al., Nucl. Phys. A524 (1991) 179.

[25] B. Lott et al., Z. Phys. A346 (1993) 201.

[26] E. Crema et al., in: Nuclear Physics at GANIL 89-91, Documentation GANIL.

[27] Review of Particle Properties, Phys. Rev. D50 (1994) 1253.

[28] W.Trautmann and the ALADIN collaboration, GSI-Nachrichten 07-93.